Final Technical Report : DE-SC0004925

Title: **Evaluating the Contribution of Climate Forcing and Forest Dynamics to Accelerating Carbon Sequestration by Forest Ecosystems in the Northeastern U.S.**

Project ID **0016636**
Proj Mgr **James M. Kuperberg**

Phone: **301-903-3511**

Division: **SC-23.1**
PI: **David R. Fitzjarrald**
Award Register#: **ER65098**

Summary

We used 10 Hz eddy flux signals and 0.2 Hz incident radiation (global shortwave and PAR) records from Harvard Forest (Massachusetts) and Tapajós National Forest (Brazil) to establish empirical relationships among directly measured cloud type and cover percentage and corresponding PAR fluctuations and its diffuse fraction. In future work such a cloud characterization will be related to water and light use efficiency estimates for each of these ecosystems.

We developed empirical relationships to link sky cover type and fraction (measured with the ceilometer) to incident direct and diffuse PAR. We developed a methodology for constructing synthetic incident solar radiation time series based on operational reports of sky cover and cloud type from National Weather Service METAR reports. The aim of this work is to document the temporal and spectral properties radiation incident on the canopy, as a first step toward developing a sky-type parameterization for the net carbon uptake models.

Work completed during this project:
1. Ceilometer estimates of cloud cover type and fraction. Cloud cover fraction has been obtained by examining the time fraction of cloud 'hits) from the ceilometer We classify cloud type by examining time series statistics from the ceilometer and the high-frequency incident PAR/incident global solar radiative flux records.

2. Developed algorithms to detect light/dark intervals in the 1Hz incident solar radiation records from the extensive archive from Harvard Forest and 3 years of data from the tropical rain forest (Brazil).

3. Found the probability density functions (*pdf*) for the length of the light and dark intervals and evaluated the validity of Lognormal and log-Lognormal distributions to describe these distributions. Three years of data have been processed to date.

4. Developed a method to quantify the standard meteorological descriptions of "broken" and "scattered" clouds in terms of the *pdf* of the light fluctuation field.

5. Made repeated trips to Harvard Forest to repair lightning damage to the suite of radiative flux measurements operated by ASRC at the EMS tower.

6. Acquired a new Linux server and hard disk array to facilitate the calculations, which had bogged down our existing Sun workstation, which is no longer being updated by the manufacturer.

7. Completed an algorithm that will generate a time series of light/dark intervals that will correspond to a given cloud state based on operational meteorological sky cover reports.

This research has been done by Sergey Kivalov and David Fitzjarrald.

1. Introduction.

The presence of clouds results in a light environment for plants that features reduced light levels, a higher diffuse fraction, altered spectral quality, characterized by alternating relatively bright and dark periods. Field measurements of CO_2 uptake over vegetated surfaces show that canopy photosynthesis is more efficient on partly cloudy days ([*Freedman et al.*, 2001; *Gu et al.*, 2002]). This phenomenon is often attributed to more uniform illumination of the canopy on such days. However, reducing light intensity also limits water stress, and fluctuating light could offer other efficiencies related to stomatal opening and closing time scales. It is difficult to assign a single cause to a complex ecosystem response. Recent model/observation studies (e.g. *Still et al.,* [2009]) sidestep these issues by treating 'clouds' as generic 'PAR reducing media'. *Mercado et al.* [2009] noted, "… the net effect on photosynthesis of radiation changes associated with an increase in clouds or scattering aerosols depends on a balance between the reduction in total PAR (which tends to reduce photosynthesis) and the increase in the diffuse fraction of the PAR (which tends to increase photosynthesis)." In cloudless conditions, aerosols alter the ratio of direct to diffuse short-wave radiation. By modulating the quality of light impinging on the ecosystem, sky condition has an important influence on the carbon uptake. Incident light variability clearly affects photosynthesis [*Whitehead and Teskey* [1995]) but it is also an important concern in understanding output photovoltaic arrays (*Giraud and Salameh* [1999]).

To examine the connections among cloud fraction and type, incident light quality, and the carbon and water exchanges, we were motivated by the following **ecological questions**:

• How does the 'cloudy day' carbon uptake depend cloud type, cloud fraction, and season?

• Are light and water use efficiencies enhanced on partially cloudy days because canopy warming and stress is relaxed by intermittent shading?

• Alternatively, does diffuse radiation, by more completely illuminating more of the canopy, lead to enhanced uptake on cloudy days?

In pursuit of these ultimate objectives, we focused this research on the following **research question**:

•What quantitative functions exist linking cloud type and fraction and incident radiation properties (diffuse/direct ratio, time fraction of direct illumination, spectral characteristics)?

This research has been done by Sergey Kivalov and David Fitzjarrald.

2. Observing clouds and incident radiation.

Falconer [1948] examined time series of daylight in the northern sky, qualitatively associating the patterns with the cloud types reported by meteorological observers. He showed that different types of clouds produce different variability of lighting conditions. Sharp current peaks in photomultiplier current showed presence of cumulus clouds; altostratus produced much smoother line. *Freedman et al.*, [2001] and *Freedman and Fitzjarrald* [2001] extended this approach, showing how sky type could be characterized using, incident downwelling global solar radiative flux and its temporal standard deviation (S_{dn} and σ_{Sdn}.). In recent years, more studies of the statistics of instantaneous and time-averaged diffuse fraction in cloudy conditions are found in the solar energy than in the ecological literature. *Suehrcke and McCormick* [1988a, 1988b] presented early versions of the probability density functions of incident light (direct and diffuse components) on cloudy days. *Woyte et al.* [2007] and *Chow et al.*,[2011] and *Lave et al.* [2011] updated this work, using wavelet analysis of fluctuations in the instantaneous clearness index, an approach we propose to follow in part. To date, characterizing sky type has been taken as a consequence of statistical analysis. The few efforts to incorporate causal influences have involved mesoscale model output.

Our effort links these approaches by including information about boundary layer development and subsequent cloudiness throughout the diurnal cycle. We classify cloud type by examining time series statistics from the ceilometer and high-frequency incident PAR record.

Duchon and O'Malley [1999] used pyranometer-averaged 1-min irradiance data to analyze response to cloud conditions. They removed a running mean and standard deviation values computed in 21-min moving window, empirically chosen. For cumulus clouds, the rapid rise in standard deviation and decrease in mean values occurred simultaneously. They found on average 45% agreement between their pyranometer method and human observations of cloud types.

Orsini et al. [2002] improved the previous researchers' methods but them by establishing new decision criteria and applying them to both solar and infrared radiation. They analyzed 10-min averages of 1-min measurements of both down dwelling and upwelling total and long wave radiations from four sensors: two pyrradiometers and two albedometers. The short wave radiation components were derived from differences between the total and long wave components. Analyzing 50-min running mean and standard deviation values, the authors received 94% success prediction rate for cirrus, 67% for cirrostratus and altostratus, and 33% for cumulus. From the long wave component, they computed cloud base height distributions, which helped with distinguishing among the polar cloud classes.

Another method to estimate cloud conditions from 5-min short wave averages is presented in *Assuncão et al.* (2007) paper. The authors estimated sky conditions for four categories: sun with cloud reflection; sun without clouds; sun partially concealed; sun totally concealed. Their method is based on the frequency distributions of clearness index for clear sky and four types of cloud cover (Weibull distributions). There is 95% correlation between the method derived relative sunshine and the shortwave irradiance observations in São Paulo, Brazil.

In this work we used Harvard Forest observations and measurements in the Amazon rainforest (LBA-EC) obtained by instruments deployed and recorded by our group to demonstrate the feasibility of defining incident light fraction from operational cloudiness data products that can be exploited by terrestrial biosphere models over large spatial domains. We note that most ecological studies do not explicitly link cloud type and cover fraction, staples of weather reports to properties of light incident at the surface. Making this connection opens the way to include operational information in studies of incident light temporal variability.

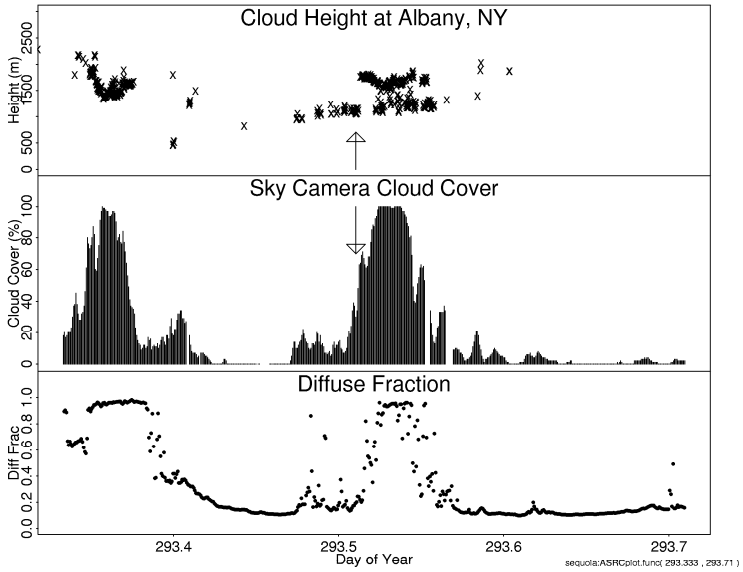

Figure 1a. Albany, NY, day 293 (19 October 2000). (top): ceilometer cloud height (m). (middle): TSI sky imager cloud cover (%). (bottom): diffuse fraction. Arrows indicate point in time (1215 LT) where images in Fig. 1b were taken and clouds are predominantly cumulus.

Fig. 1b. (top): TSI unprocessed and (bottom) processed image at 1215 LT for 19 October 2000.

A case illustrates the link between cloud cover and incident solar radiation (Figure 1). Ceilometer estimates of cloud base to indicate cloud cover fraction found using the whole-sky camera. The diffuse fraction remains small during the partly cloudy morning of the central day in the plot, increasing to nearly 1 as the sky became overcast. In our work, we classify cloud type by examining time series statistics from the ceilometer and high-frequency incident PAR record. Separating boundary layer cumulus, a direct local consequence of surface heat and moisture flux convergence into the lower atmosphere, from generic cloud cover will become important as coupled atmosphere/land surface models are exercised at increasingly higher resolution. . The most promising sky types for vegetation sensitivity are likely to be the forced cumulus situations studied in [*Freedman et al.*, 2001; *Freedman and Fitzjarrald*, 2001].

We made measurements of cloud base along with high time resolution incident solar radiation measurements at a tropical forest site in Brazil (Figure 2). The regularity of the tropical environment (Figure 3) leads to a repeatable sequence of forced cumulus development in late morning. This makes for an ideal laboratory to study links between measured cloudiness and its consequence on surface radiative fluxes.

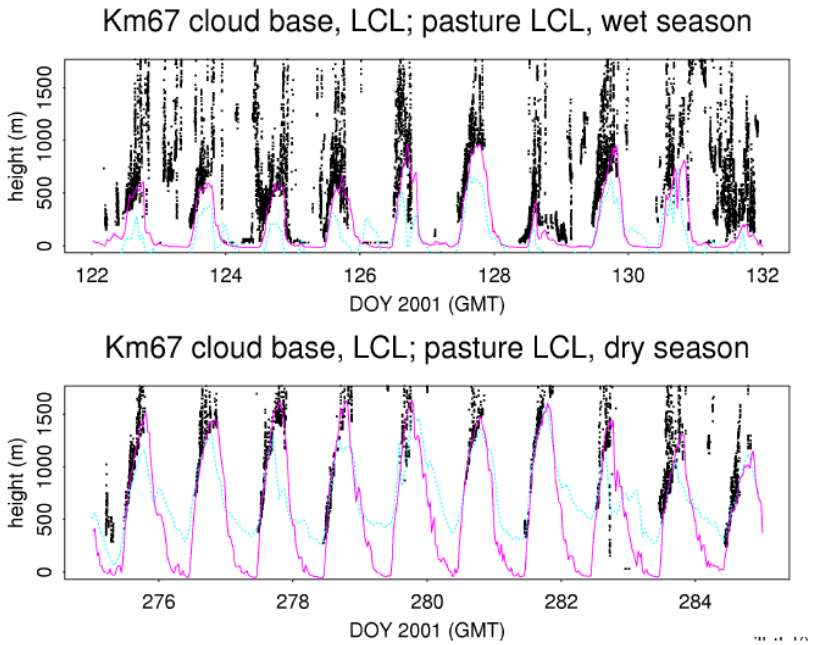

Figure 2. Top panel: Cloud base at km67 Brazil (black), lifting condensation level (LCL) at km67 (blue), and LCL at km77 (purple) during a wet season period in 2001 (May 2-11, days 122-131). Bottom panel: As in top panel but for a dry season period in 2001 (October 2-12, days 275-285). LCL at km77 (a cleared agricultural site) corresponds to the km67 cloud base better than does local LCL at km67 (an old-growth forest site).

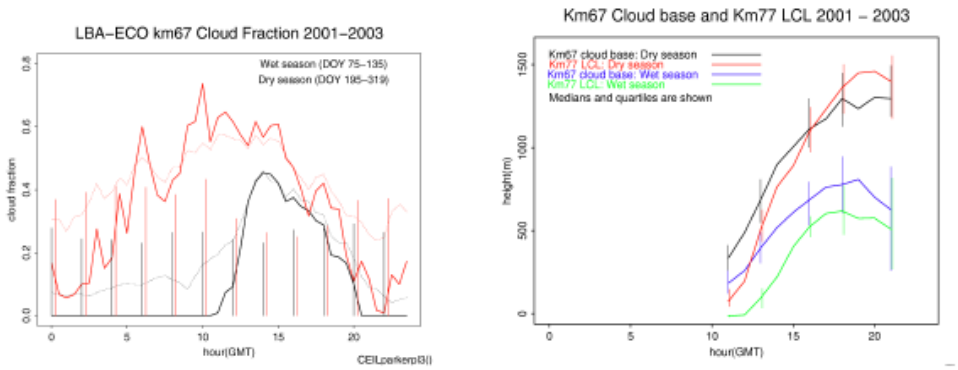

Figure 3. Left: Hourly median & mean (dashed) cloud cover fraction at km67 for the wet season (red) and dry seasons 2001-2003 (bars indicate quartiles). Note the absence of nocturnal dry season clouds. Right: The bars denote the quartiles. The cloud base during dry season afternoons is ≈1300m; during wet season ≈ 750m. The km77 LCL corresponds well to the km67 cloud base during the dry season, but slightly underestimates in the wet season.

Our effort concentrated first on defining the probability density function of light and dark intervals on partly cloudy days. Then we quantified what is meant by "scattered" and "broken" cloud fields, typically reported by weather observers and the National Weather Service automatic weather stations (ASOS), in terms of the temporal qualities of incident radiation.

To generate 'artificial sky patterns' (see below) we started with methodology described by *Beyer et al.* [1994]. *Suehrcke and McCormick* [1988a; 1988b] presented early versions of the probability density functions of incident light (direct and diffuse components) on cloudy days. [*Woyte et al.*, 2007] updated their work, introducing wavelet analysis of fluctuations in the instantaneous clearness index.

3. Light and dark periods in Brazil and at Harvard Forest.

At an old-growth forest site of LBA-ECO (Km67), located in the Tapajos National Forest off Kilometer 67 of BR-163 south of Santarem, a Vaisala CT-25K ceilometer was installed in April, 2001 and remained operational through June, 2003. The ceilometer provided 15-second measurements of cloud base (three levels up to 7500 m), echo intensity, and a 30-m resolution backscatter profile. Global long-, short- and PAR radiation upwelling and downwelling were recorded at 5 s intervals (Figure 4).

At an old-growth forest near Petersham Massachusetts Global long-, short-wave and PAR radiative fluxes (upwelling and downwelling) have been were recorded at 1 s intervals since 1994. Light and dark periods measurements were extracted and a threshold 0.8 of the clear sky was used to identify cloud-shaded periods (Figure 5).

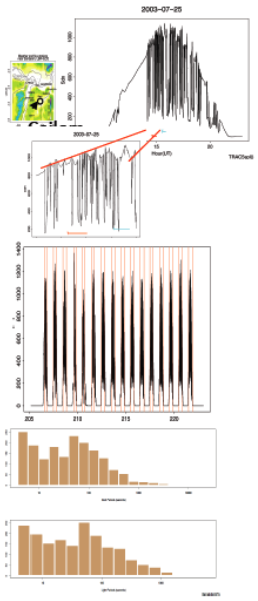

Figure 4. Tapajós National Forest, Brazil. Top column left: Location map; Top right: Example of incident short-wave radiation. Second column: expanded view. Third column: sequence of 16 selected days. Fourth column: histogram of light intervals. Fifth column: histogram of dark intervals.

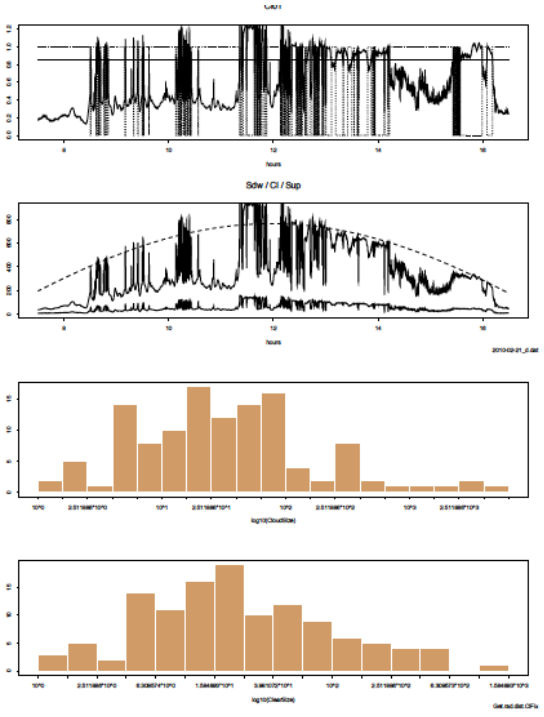

Figure 5. Harvard Forest MA. Top: Example of one day of filtered incident solar radiation; Second row: Raw data; Third row: histogram of 8 days of light periods; Fourth row: histogram of corresponding dark intervals.

Statistics of cloud cover estimates.

We estimated the statistical relationships between the cloud and clear area sizes and between the sizes of the light and dark passes and connect them to the cloud cover change

Assuming that the convective clouds are circular and uniformly distributed over the sky and that the wind in the cloud base is stationary over the small time interval when a set of clouds passes over, we derived the following expressions connecting cloud diameter *D*, measured cloud size (dark pass) *d*, distance between clouds *L*, and measured path (light pass) *l*:

$$(D+L)^2 = \frac{4}{\sqrt{3}} Dl \qquad \Rightarrow \qquad L = \frac{2}{\sqrt[4]{3}}\sqrt{Dl} - D = \frac{2}{\sqrt[4]{3}}\sqrt{\frac{d}{\alpha}l} - \frac{d}{\alpha},$$

where $\alpha = d/D \approx 0.849$ is equal to the mean ratio value.

The change between scattered and broken cloud conditions occurs when the areas of clouds and free space among them are equal to each other, occurs when:

$L = 0.346D.$

For the consecutive light and dark periods, we received the alternate formula for the measured *d* and *l*:

$$l \approx 0.8857\frac{d}{\alpha} \approx 1.043d.$$

This formula is valid for the nonstationary slowly variable winds because it represents the ratio between the consecutive light and dark periods and doesn't specify their actual sizes, which will of course depend on the actual wind speed.

4. Parameterizing Irradiance

Because of large variability of the light and dark periods, it seems to be practical a selective approach when only one type of clouds is chosen based on METAR data and/or the measured *d* and *l* sequences.

In our current research we are going to follow this approach and look though the couple years worth of irradiation data from Harvard Forest. Then we generate the light and dark distributions over this large time interval.

Clear sky irradiance parameterization

We incorporated the clear sky fit into the algorithm to retrieve the light and dark sequences. Unless there were no clear sky interpreted data in the daytime measurements, this helped to better position the curve over the real data. However, if two days or more are joined together for this analysis, there is usually enough information to fit this curve over the data.

Originally, in single-day studies we used the simple equation for the insolation parameterization as in *Kalisch and Macke* [2008]:

$$Q_{SW} = S_0 \cdot \cos z \cdot T,$$

where S_0 is the solar constant, z is the zenith angle, and T is the atmospheric transmittance.

We did not use any water vapor correction in this calculation; the transmittance coefficient was calculated by the non-linear best fit in the *Splus* package, intrinsically absorbing all the changes in the environment. The resulting clear sky fit was generally good in around noon, but yielded overestimates both during the morning and afternoon hours.

One approach is to keep the same equation but change the way to define *Kalisch and Macke* [2008] derived T from the water vapor partial pressure at the ground level by *Zillman* [1972]:

$$T_0 = \frac{\cos z}{(\cos z + a) p_w 10^{-3} + b \cos z + c},$$

in which a = 2.7, b = 1.085, and c = 0.1. The authors presented cases where this approach overestimates the clear sky irradiation for broken cloud conditions. They optimized the coefficients to reduce the systematical errors with their 2006 cruise data and found that Zillman's parameterization is useful for the calculating short-term fluctuations.

For this study, we use a more natural approach following the exponential law of extinction in atmosphere. The intensity of the passing through the atmosphere irradiation is a subject to Bouguer extinction law:

$$I = I_0 \cdot e^{-A \cdot M(z)},$$

where I, I_0 are the light intensities, *M(z)* is the relative air-mass number, z is the zenith angle, and A is the extinction coefficient.

The $A \cdot M(z)$ is also named as optical thickness or optical depth (*McCartney* [1976]), which generally depends on the wavelength of light. For the relative air-mass estimation, we accommodated Andrew Young's approximation formula *Young* [1994], derived for 678 nm wavelength (red light) for consistency with the air-mass table from 1972 International Organization for Standardization standard atmosphere (ISO) Standard Atmosphere (1972).

For the horizontal irradiance I_H the *cos(z)* is included in the law of extinction:

$$I_H = I_0 \cdot \cos(z) \cdot e^{-A \cdot M(z)}.$$

We used these algorithms to recover cloud fraction, temperature, dew point, pressure, and wind vector from the earlier METAR files.

5. Statistics of light and dark intervals at two forest sites.

The samples of the spectra of light and dark generated for month of February and July were used in *Fitzjarrald and Kivalov* [2012]. We focused on two ecosystems in FLONA-Tapajós, Brazil and Harvard Forest, MA. We used our modified software to analyze the highly variable days over the month time span and derive the light and dark period histograms from the data.

Figures 6 and 7 show 5 days from Harvard Forest of 16 days from Brazil.

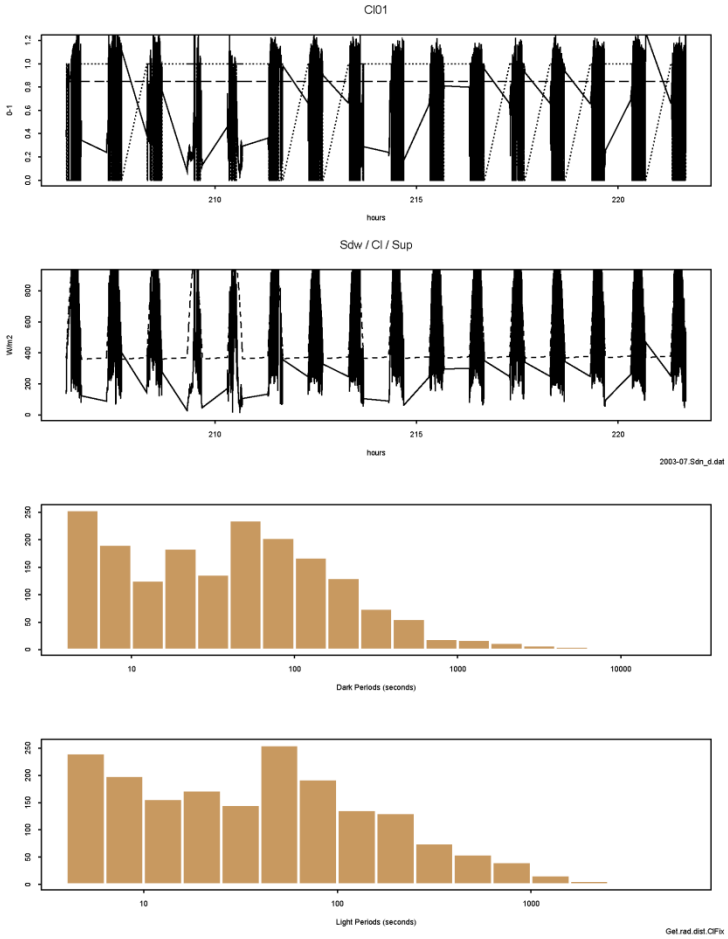

Figure 6. Spectra of light and dark intervals generated for 16 July days at the Tapajós National Forest site, Brazil.

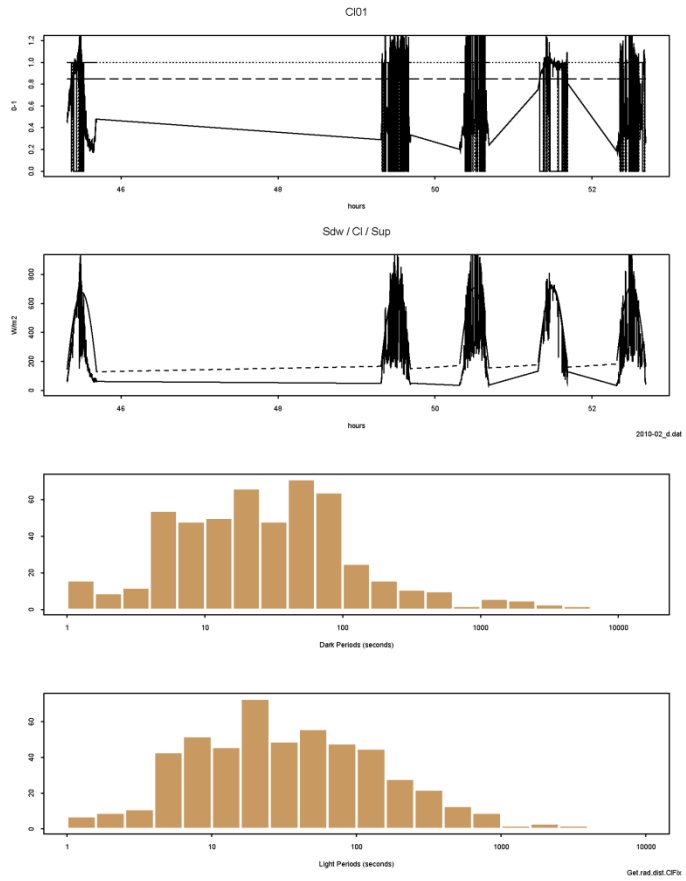

Figure 7. Histograms of the duration of light and dark intervals generated for 5 February days at Harvard Forest.

The Lognormal distribution to describe the light and dark intervals for broken and scattered cloud conditions.

We seek to link cloud classification used in operational meteorology and widely available to the temporal properties of light and dark intervals as observed at the ground.

Our initial approach was to parameterize by the *pdf* of the light and dark intervals using the Lognormal distribution. These cases give evidence of Lognormal distributions in both light and dark series for both sites, consistent with the work of López et al. (1977) on Lognormal distributions of cumulus cloud sizes. We expected that their advection over a site would produce a similar shade pattern. The Lognormal *pdf* is:

$$f(x) = \frac{1}{\sqrt{2\pi}Sx} e^{-\frac{(\ln(x)-M)^2}{2S^2}},$$

where M and S are the parameters.

The mean, variance, skewness, and kurtosis of the distributions can be derived from M and S by the formulas:

$$\mu = e^{M+S^2/2},$$

$$\sigma^2 = e^{S^2+2M}\left(e^{S^2}-1\right),$$

$$\gamma_1 = \sqrt{e^{S^2}-1}\left(2+e^{S^2}\right),$$

$$\gamma_2 = e^{4S^2}+2e^{3S^2}+3e^{2S^2}-6$$

The fits of the log-normal distributions into the multi-year histograms of the light and dark periods for both the Scattered and Broken cloud conditions are presented in the following Figures.

The histograms and the distributions are placed over the logarithmic time scale. The vertical lines in the graphs are the distribution mean values and the standard deviation intervals (in seconds) around the means.

Scattered cloud conditions:

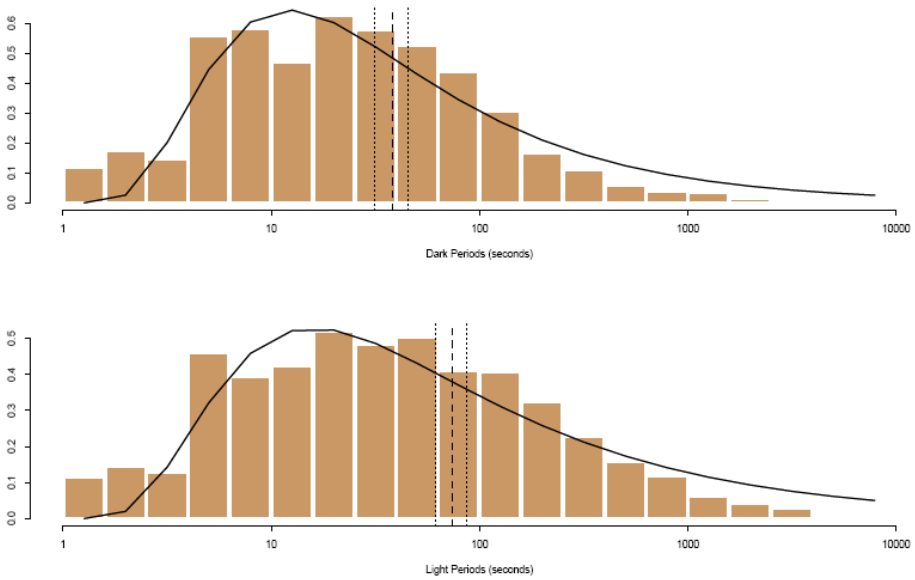

Figure 8. The log-normal *pdf* fits into the multi-year histograms for *scattered cloud* conditions

	Dark period	Light period
M	0.33162	0.47809
S	0.50504	0.54233
μ 10^{μ} (seconds)	1.58274 (38.25992)	1.86855 (73.88426)
σ 10^{σ} (seconds)	0.85314 (7.13089)	1.09267 (12.37871)

Table 1. Parameter values for the *scattered cloud* distributions in Figure 8.

Broken cloud conditions:

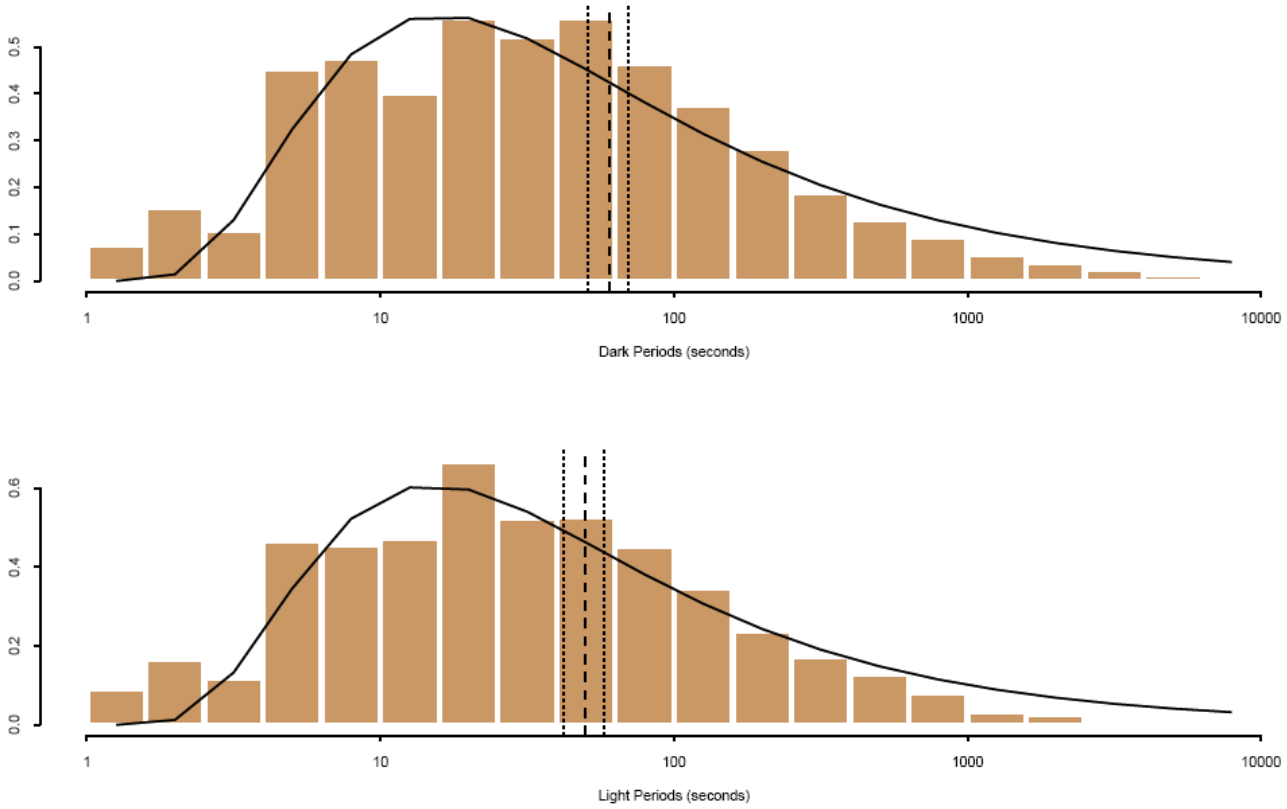

Figure 9. The log-normal pdf fits into the multi-year histograms for *broken cloud* conditions

	Dark period	Light period
M	0.44681	0.40866
S	0.51181	0.49249
μ 10^{μ} (seconds)	1.78208 (60.54527)	1.69883 (49.98475)
σ 10^{σ} (seconds)	0.97521 (9.44513)	0.89006 (7.76367)

Table 2. Parameter values for *broken cloud* distribution illustrated in Figure 9.

From these short samples, there is some evidence for Lognormal distributions in both light and dark series for both sites. This is consistent with the works of López et al. (1977) on Lognormal distributions of cumulus cloud sizes. However, below we show that further work demonstrated that in most cases a better description fitted the long duration samples from Harvard is actually the Weibull distribution.

The clear sky correction applied for multiple months.

During the clear sky fitting, we saw that the atmospheric extinction slightly varies every day, and it varies significantly from month to month. The clearest months are in the winter with $A < 0.04$, and the haziest months are in the summer with $A > 0.16$. We need to make sure that our 0.85 (15%) threshold from the clear sky values we use to distinguish between light and dark is not going to be compromised by the month-by month irradiation change due to A change. Table 3 shows the annual differences in irradiation for the different air masses = zenith angles due to the extinction coefficient change.

Air-mass	$M(z)$	1.154	1.42	2	3	4
zenith angle	z	30	45	60	71	76
A=0.04	$e^{-A \cdot M(z)}$	0.954889	0.944783	0.923116	0.88692	0.852144
A=0.166	$e^{-A \cdot M(z)}$	0.825667	0.790002	0.717487	0.607745	0.514788
annual difference	I	13.5%	16.4%	22.3%	31.5%	39.6%

Table 3. Differences in irradiation for the different air masses

For the zenith angles > 45°, annual differences in the clear sky irradiance exceed 16%, over our 0.85 threshold. We must introduce some flexibility into the extinction with an additional haze coefficient: $coeff_h$. This is done by using the formula similar to the standard one used in the clear sky model for the sun elevation:

$$coeff_h = C_1 - C_2 \cos\left(\frac{2\pi}{365.25}(DOY - C_3)\right).$$

Then the law of extinction for the horizontal irradiance will be modified as following:

$$I_H = I_0 \cdot \cos(z) \cdot e^{-A_1 \cdot coeff_h \cdot M(z)},$$

where A_1 is a correction coefficient, which should be near unity in ideal case.

Table 4 presents the extinction coefficient (A) values of the clear sky fitting for 2008, 2009, 2010, and 2011. We filtered extreme values of extinction values by applying a 95% confidence interval. The last row of the table shows the best fit into the $coeff_h$ formula above.

Table 4. Extinction coefficient (A) values

	Jan	Feb	Mar	Apr	May	Jun	Jul	Aug	Sep	Oct	Nov	Dec
2008	0.0507 ±0.004	0.0504 ±0.002	0.0829 ±0.002	0.1315 ±0.012	0.1629 ±0.015	0.1569 ±0.01	0.1668 ±0.007	0.1533 ±0.009	0.1371 ±0.012	0.0918 ±0.006	0.0667 ±0.007	0.0603 ±0.005
2009	0.0463 ±0.008	0.0474 ±0.004	0.0830 ±0.007	0.1164 ±0.009	0.1593 ±0.008	0.1595 ±0.011	0.1486 ±0.014 (few data)	0.1510 ±0.008	0.1358 ±0.005	0.0865 ±0.012 (few data)	0.0763 ±0.002	0.0529 ±0.002
2010	0.0374 ±0.003	0.0458 ±0.003	0.0845 ±0.006	0.1069 ±0.004	0.1718 ±0.011 (few data)	No data	0.1663 ±0.008 (few data)	0.1685 ±0.014 (few data)	0.1322 ±0.004	0.1044 ±0.003	0.0676 ±0.004	0.0554 ±0.003
2011	0.0436 ±0.003	0.0408 ±0.005	0.0821 ±0.005	0.1222 ±0.01 (few data)	0.1626 ±0.008							
coeff	0.0442	0.0583	0.0841	0.1179	0.1481	0.1683	0.1719	0.1582	0.1305	0.0977	0.0667	0.0476

Figure 10 shows the best fit of the data from the Table 2 into the $coeff_h$ formula above with coefficients $c1$=0.10805, $c2$=0.06461, and $c3$=5.74010.

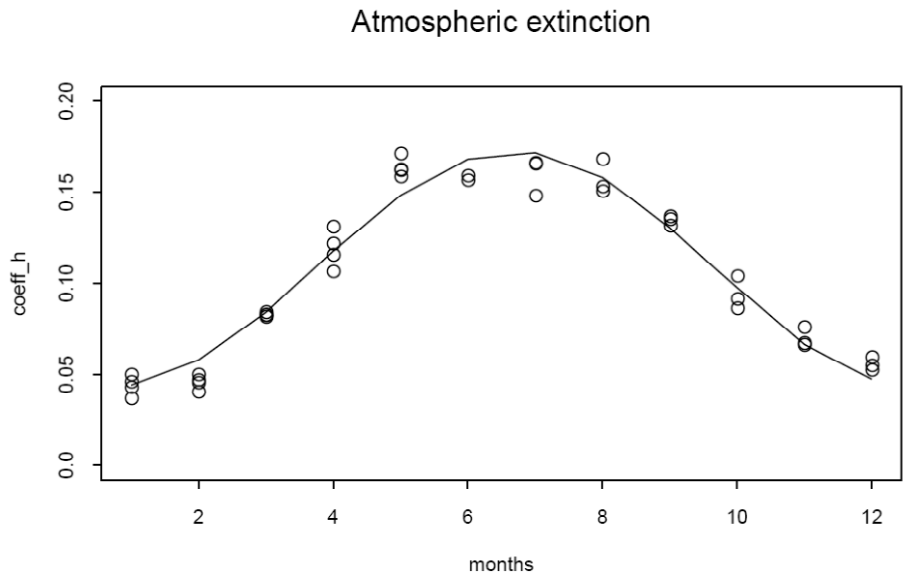

Figure 10. $coeff_h$ best fit of the data from the Table 4.

6. Analyzing the long-term record from the Harvard Forest site.

In this section we focus on distributions of cloud induced incident light fluctuations. To achieve its goal, the analysis of the single point ground measurements of incident light is conducted on the 0.2 Hz short wave irradiation data from Harvard Forest for multiple years. We refine the approach to incorporate operational meteorological cloud cover and sky descriptions into the analysis. The distinction between the cloud conditions and levels is done by using data from closest METAR stations: KORE and KORH and by lifting condensation level calculations. We present the distributions of light and dark for the *scattered* and *broken* clouds as well as for the low and mid-upper cloud layers.

Data sources

The radiation data to analyze is collected from Harvard Forest Tower. This is 30 meter Eddy Flux Tower set up in 1990, and it is a part of Environment Measurement Station located at Harvard Forest near Petersham, MA. In this research, we use 6 years (from 2006 to 2011) of 1 Hz irradiation measurements from the Harvard Forest Tower combined with 10 Hz flux measurements from other sources into the 1-second raw files.

The direct cloud fraction measurements estimated by ceilometers is the main reference for our research comparison. To do this, we use the METAR-ASOS data from the NCDC database (METAR). For the cloud cover, the METAR standard is following: FEW (1/8 TO 2/8 cloud coverage); SCT (SCATTERED, 3/8 TO 4/8 cloud coverage); BKN (5/8-7/8 coverage); OVC (OVERCAST, 8/8 Coverage).

The closest two METAR-ASOS sites are the Orange Municipal Airport, MA station (KORE) (The same station was used in Freedman et al. (2000) with Harvard Forest) and KORH – Worcester Regional Airport, MA. Even though KORE is closer to Harvard Forest than KORH, the KORH is to the south at higher elevation; KORE is to the northwest. So from the irradiation point of view, the KORH cloud condition might be more representative than KORE ones. This can be justified by the solar geometry for northern hemisphere that the direction to sun is to the south of the observer on the ground, so the fluctuation of downwelling irradiance will be due to the clouds to the south on the station. This south shift will depend on the cloud base height. In the summer time, the solar elevation will be up to 70 degrees so that south shift will be small, but in the winter, when the sun is just 20 degrees above the horizon, it can be significant. So KORH could give better relevant cloud estimations than KORE for this time frame.

Data preparation

In this data analysis, the 1-second shortwave radiation data was normalized against the calculated clear sky irradiance. This normalization helps to exclude from the considerations the light variability due to the daily clear sky irradiance change and keep only the light variability induced by the atmosphere. The normalized irradiance data values are generally between 0 and 1, but they can increase above 1 (the clear sky threshold) when the reflections of light from the edges of the low-level cumulus clouds occur (Lianhong Gu et al.(2001), Segal, M. & J. Davis (1992)).

An example of the processing approach (Figure 11) shows the raw data clearly presenting the clear sky outer irradiation envelope (dashed line) and the inner irradiation envelope associated with the cloudy conditions.

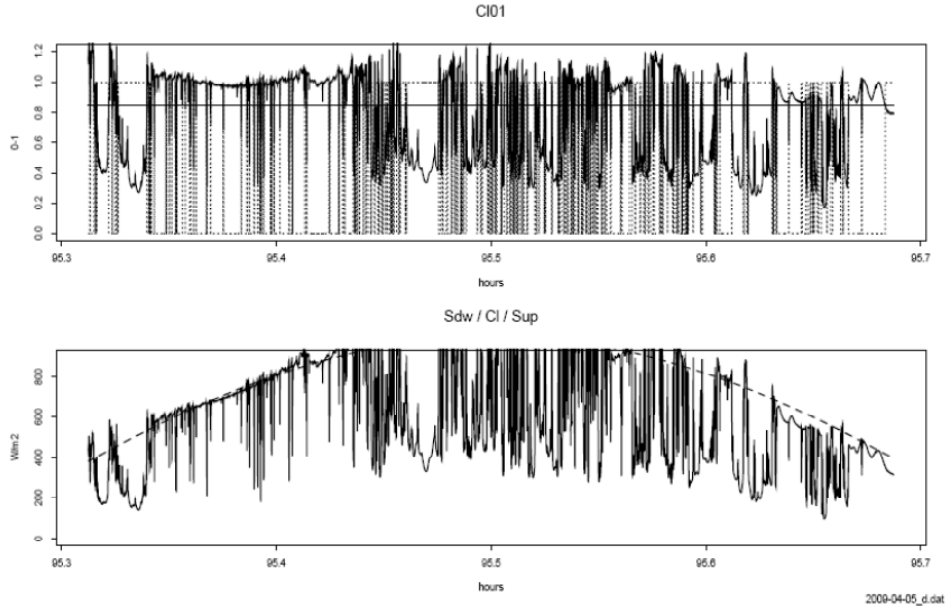

Figure 11. A single day of 1-second incident shortwave radiative flux. Top: Normalized series; Bottom: Raw data before normalization.

We distinguished dark and light periods by applying the threshold of 0.8 to the normalized 1-second data. The choice of the threshold can be justified by the magnitude of the fluctuations of normalized 1-second data between 0.4 – 0.5 and 1.1 – 1.2, such that 0.8 is approximately the median of the data.

The signal undergoes nearly instantaneous jumps back and forth across the threshold. The relatively long period above the threshold is associated with the single clear-from-cloud period, and the continuous period below the threshold is associated with the single cloud passage. Duration of the cloud passes are conveniently represented by the number of data points therein.

Data in Figure 12 demonstrate that both *scattered* and *broken* cloud conditions introduce different lighting regimes and these must be treated separately. To do this, we use conventional National Weather Service METAR data from the KORE and KORH stations discussed earlier and filter for consistent conditions at both sites. This ensures that we are within some homogeneity of cloud condition above the Harvard Forest site.

7. Multiple year data analysis

Applying the described technique to the 6 years of 1-second data (from 2006 to 2011) brought the following combined histograms of the distributions of light and dark periods by their lengths in seconds.

All-level cloud condition analysis: superiority of Weibull distribution

The first group of graphs is for the scattered cloud conditions represented by 20378 cases, and the second group of graphs is for the broken cloud conditions represented by 8912 cases.

Scattered clouds prevail	Broken clouds prevail
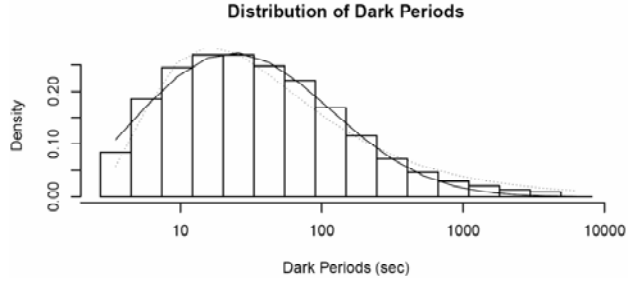	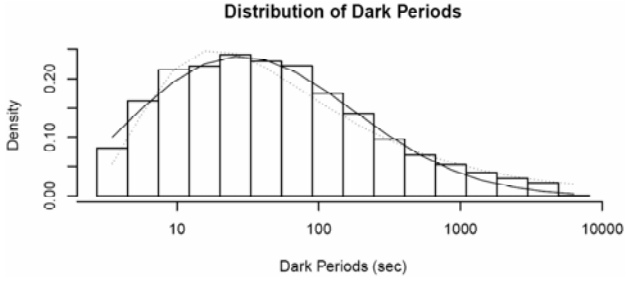

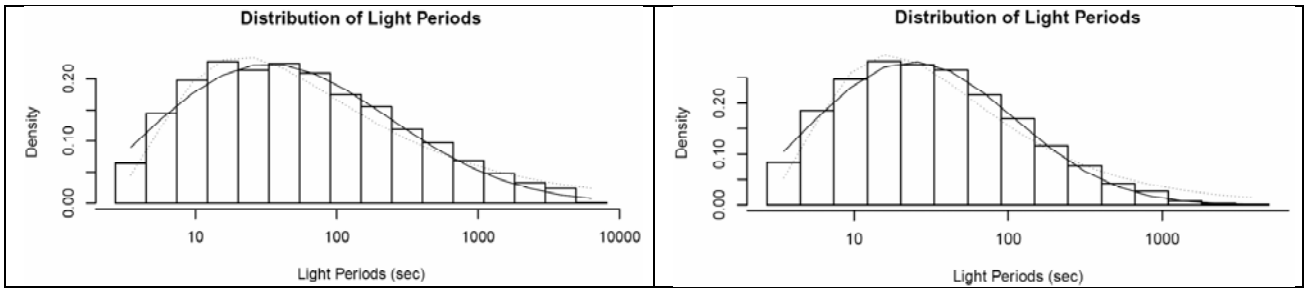

Figure 12. Left: distribution the scattered cloud conditions ; Right distribution for broken cloud conditions.

The following Table presents the means and standard deviations of the originally selected data.

Scattered clouds prevail		Broken clouds prevail	
clear	mean=234.180 std=557.177	clear	mean=85.8718 std=191.693
cloud	mean=125.382 std=370.451	cloud	mean=206.262 std=545.718

The two lines on the Figures are the best fits of the Weibull (solid line) and Lognormal (dotted line) distributions into the histograms of the distributions. It is easy to see that for the times below 2000 seconds, the Weibull *pdf* fit is better than the Lognormal one. Due to its shape, the Lognormal *pdf* fits make overestimations of occurrence of the short light and dark periods around 10 – 40 seconds, and underestimations of occurrence of the middle light and dark periods around 60 – 1000 seconds. They become closer but still with the overestimations of occurrence of the longer light and dark periods above 2000 seconds. On the other hand, the Weibull *pdf* fits better resemble the overall shapes of the histograms with some underestimations of occurrence of the longer light and dark periods above 1000 seconds.

The same conclusions give Kolmogorov-Smirnov goodness of fit tests performed on the Weibull and Lognormal pdf fits in our R programs. The following Table shows the results of the K-S tests for the fits above.

	Scattered clouds prevail		Broken clouds prevail	
Lognormal	clear	S= 0.06393394 P= 0	clear	S=0.05777095 P= 0
	cloud	S= 0.05220196 P= 0	cloud	S=0.05587026 P= 0
Weibull	clear	S=0.01482499 P=0.00017471	clear	S=0.01548434 P=0.02350232
	cloud	S=0.01920975 P=4.0840e-07	cloud	S=0.02041007 P=0.00085514

The K-S goodness of fit statistics are at least twice lower for the Weibull pdfs than for the Lognormal pdfs, and confidence probabilities are above 0. This concludes that for the presented combined cases, the Weibull pdf fits are better than the Lognormal pdf fits for both light and dark pass lengths and for both Scattered and Broken cloud conditions.

Strict separation by cloud level analysis

The cloud levels are distinguished by using the calculated lifting condensation level (LCL) by Freedman, J.M. et al.(2000). To make the clear distinction between the levels, the LCLs for two sites KORE and KORH were used simultaneously. For the low-level clouds, the only data with the cloud heights below LCLs*1.3 and below 2000 m was considered to belong to the convective clouds above the Convective Boundary Layer. For the mid-upper level clouds, the only data with the cloud heights above LCLs*1.3 was chosen to belong to middle and upper layers.

The main representation of clouds in these levels is the following. For the low-level (below 2000m), there are fair weather Cumulus, which are the Convective Boundary Layer induced convective clouds, developed from them Cumulonimbus (thunderstorms), and Stratocumulus and Nimbostratus (overcasts). For the mid-level (from 2000 to 6000m), there are Altocumulus (convective on the middle level, cold front advancing) and Altostratus (approach of a warm front, overcasts).

Similar combined histograms as above but separated for two cloud levels are presented in Figure 13.

Low-level clouds	Mid-upper level clouds
Scattered clouds prevail	Scattered clouds prevail
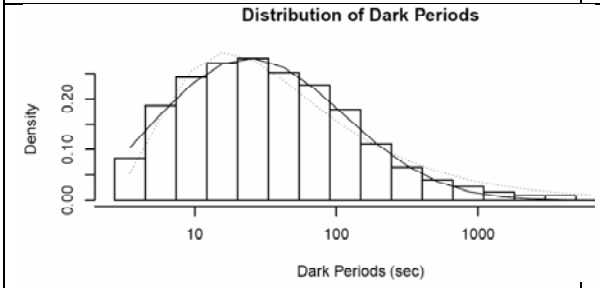	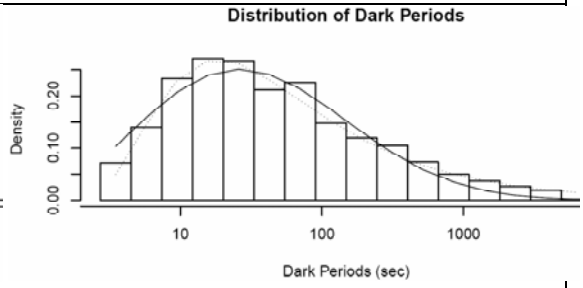
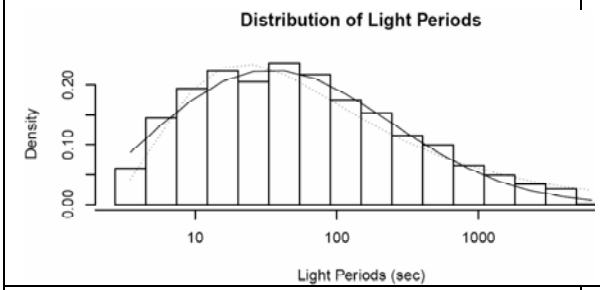	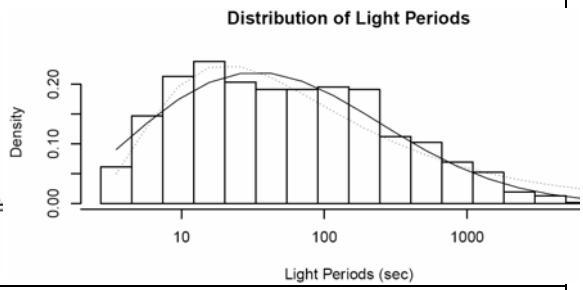
Broken clouds prevail	Broken clouds prevail

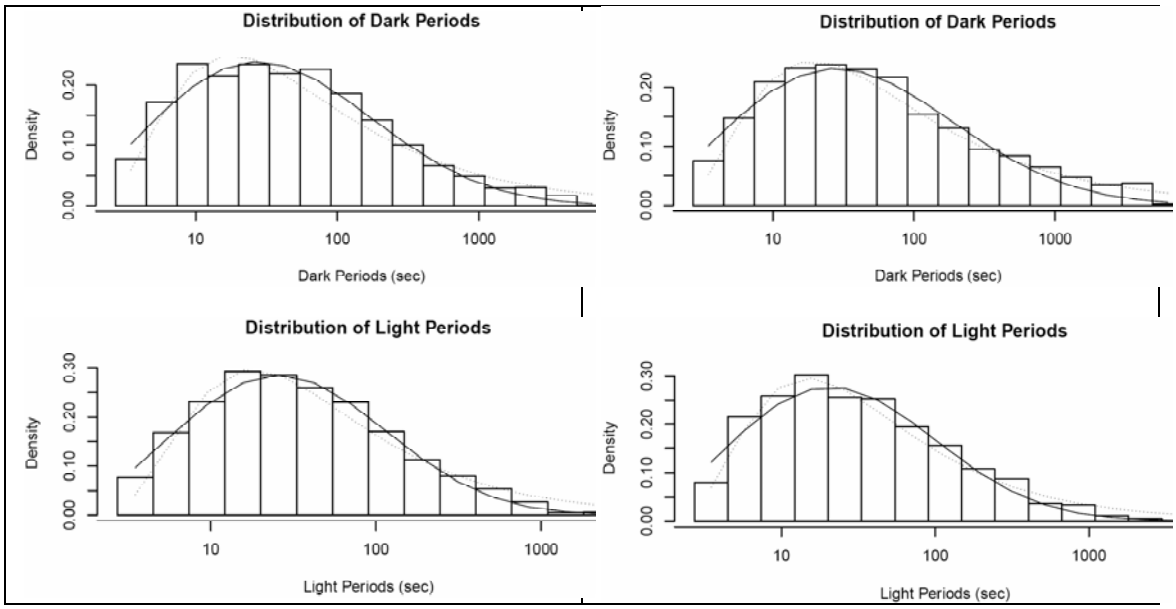

Figure 13. Combined histograms as above but separated for two cloud levels.

Low-level clouds		Mid-upper level clouds	
Scattered clouds prevail		Scattered clouds prevail	
clear	mean=240.478 std=576.282	clear	mean=208.4227 std=486.668
cloud	mean=113.533 std=345.263	cloud	mean=191.9706 std=519.558
Broken clouds prevail		Broken clouds prevail	
clear	mean=88.2070 std=186.746	clear	mean=91.58089 std=212.320
cloud	mean=186.818 std=501.570	cloud	mean=261.9054 std=683.577

Table 6. Means and standard deviations of the originally selected data separated by cloud levels.

The presented graphs feature the same types of histograms and fits as in the all-level cloud condition case. The Weibull fits are the solid lines; Lognormal fits are the dotted lines. The low-level cloud case shows the same features with the all-level cloud case with the generally better fittings of the light and dark histograms by the Weibull *pdf*. However, the mid-upper level cloud case doesn't follow the same pattern as the low-level and all-level cloud cases. For the dark passes, it shows more skewed and fatter tailed distributions those could be more suitable for the Lognormal fits than for the Weibull ones.

The similar conclusions give the Kolmogorov-Smirnov goodness of fit tests performed on the separated by cloud level data. The following Table presents the K-S statistics and confidence probabilities for the Weibull and Lognormal fits for each cloud level.

Low-level clouds				
	Scattered clouds prevail		Broken clouds prevail	
Lognormal	clear	S= 0.06173337 P= 0	clear	S=0.05514045 P=6.3989e-08
	cloud	S= 0.0598134 P= 0	cloud	S=0.06411985 P=1.0908e-10
Weibull	clear	S=0.01412341 P=0.02480259	clear	S=0.01866348 P=0.2500152
	cloud	S=0.01690931 P=0.00440223	cloud	S=0.02269663 P=0.09064011
Mid-upper level clouds				
	Scattered clouds prevail		Broken clouds prevail	
Lognormal	clear	S=0.08056974 P=1.4174e-07	clear	S=0.05129616 P=6.8412e-05
	cloud	S=0.0339844 P=0.1073872	cloud	S=0.04716372 P=0.00028206
Weibull	clear	S=0.02834449 P=0.2386451	clear	S=0.02855647 P=0.07428998
	cloud	S=0.03828326 P=0.03983675	cloud	S=0.0368747 P=0.006728118

Table 7. K-S statistics and confidence probabilities for the Weibull and Lognormal fits for each cloud level

It is seen that the Weibull *pdf* better fits the low cloud level light and dark passes than the Lognormal one, and the same is correct for the mid-upper cloud level light passes. But for the mid-upper cloud level dark passes, there is just a slight advantage to use the Weibull fit over the Lognormal one for broken cloud conditions. And for the scattered cloud conditions, the Lognormal fit for the mid-upper cloud level dark passes looks preferable over the Weibull one.

The restrictions imposed on the cloud level data selection put out of considerations all cases with detected by both KORE and KORH ceilometers mixes between low and mid-upper level clouds. It happened that for broken cloud conditions from 8912 cases in total, 2864 were chosen for the low-level and only 1947 were chosen for mid-upper level, and for scattered cloud conditions from 20378 cases in total, 10581 were chosen for the low-level and only 1258 were chosen for mid-upper level. So due to low numbers of available cases, the mid-upper level data for both scattered and broken cloud conditions can be underrepresented to make clear statistical decisions on the best fits.

Multiple cloud levels analysis

Finally we look at the cases where the clouds present on both cloud levels for at least one of the sites. For broken cloud conditions from 8912 cases in total, there are 2373 cases satisfying these criteria, and for scattered cloud conditions from 20378 cases in total, there are only 418 cases respectively.

Scattered clouds prevail	Broken clouds prevail
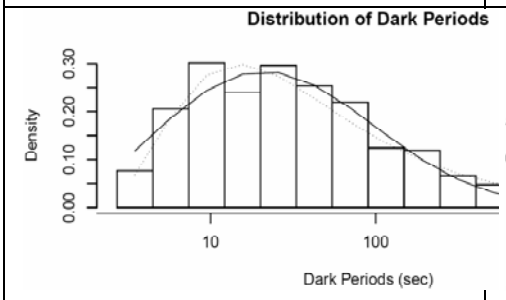	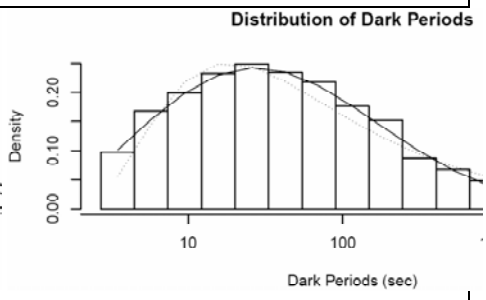

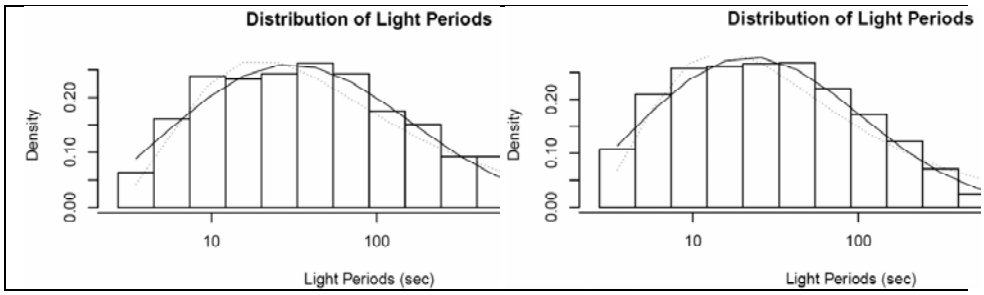

Figure 14. Combined histograms as above but for *scattered* and *broken* cloud conditions.

Scattered clouds prevail		Broken clouds prevail	
clear	mean= 110.2506 std= 217.922	clear	mean= 68.8129 std= 126.016
cloud	mean= 91.9521 std= 220.398	cloud	mean= 167.357 std= 419.893

Table 8. Means and standard deviations of the originally selected data.

The presented graphs show the consistency with both the all-level and the low-level cloud cases with the generally better fittings of the light and dark histograms by the Weibull pdfs. Even though the number of periods is small for the scattered cloud conditions, the Weibull pdfs fit very well in the histograms of both light and dark passes as well.

The same conclusions give Kolmogorov-Smirnov goodness of fit tests.

	Scattered clouds prevail		Broken clouds prevail	
Lognormal	clear	S=0.08108483 P=0.00973136	clear	S=0.08258132 P=2.6090e-14
	cloud	S=0.0555088 P=0.148404	cloud	S=0.06908216 P=7.8624e-10
Weibull	clear	S=0.03292917 P=0.7591014	clear	S=0.02102211 P=0.2366273
	cloud	S=0.03832949 P=0.5317434	cloud	S=0.01455967 P=0.6937822

Table 9. K-S statistics and probabilities for the fits in Figure 14.

The K-S statistics are much lower for the Weibull *pdf* than for the Lognormal, and confidence probabilities are much higher for the Weibull fits. In the agreement with the observations above, this also concludes that for the mixed cloud level only cases, the Weibull fits are better than the Lognormal ones.

8. Generating synthetic time series for given cloud conditions

The statistical analysis of the data showed that the Weibull distributions are the better fits for all pass lengths but for scattered cloud conditions when no low-level clouds are presented. So in simulating 1-second time series of the fluctuating light for different cloud conditions, we use the best fits using the Weibull *pdf*. The results of simulations are presented on the following figures. To make the distinctions, each

Figure presents two independently generated time series. It can be seen that the all-level, low-level, and mixed level cloud simulation cases feature more rapid light fluctuations than the mid-upper level cloud simulation. This is in the agreement with the cloud types presented on the different levels. This also signifies that the most rapid light fluctuations are due to the presence of the low-level clouds

.

All-level cloud condition

Scattered clouds prevail	Broken clouds prevail

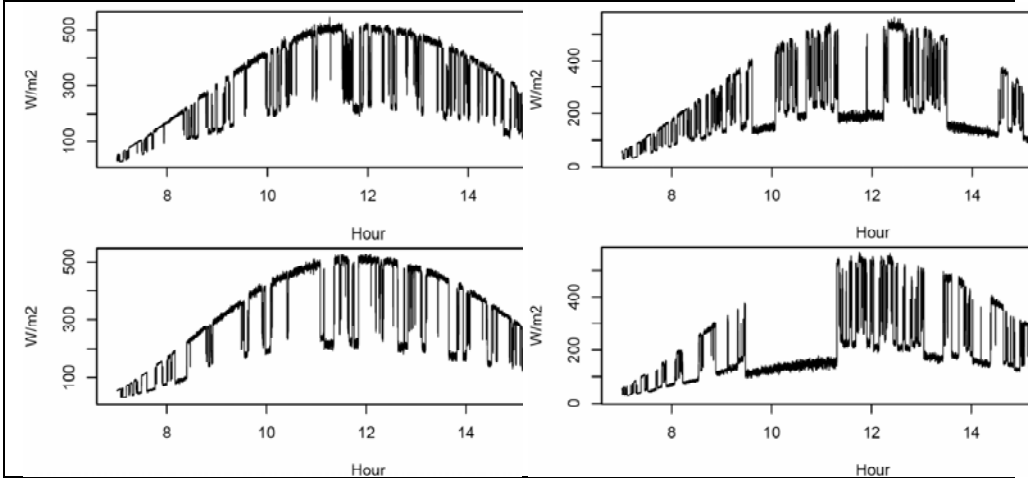

Figure 15. All-level sky condition synthetic time series.

Low-level cloud condition

Scattered clouds prevail	Broken clouds prevail

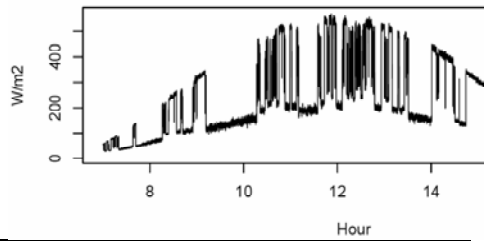

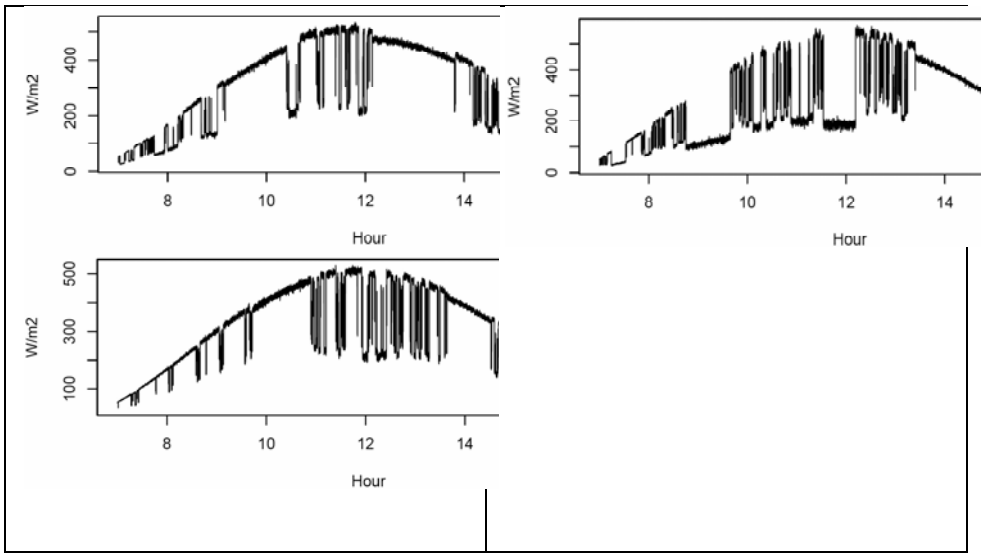

Figure 16. Low-level sky condition synthetic time series.

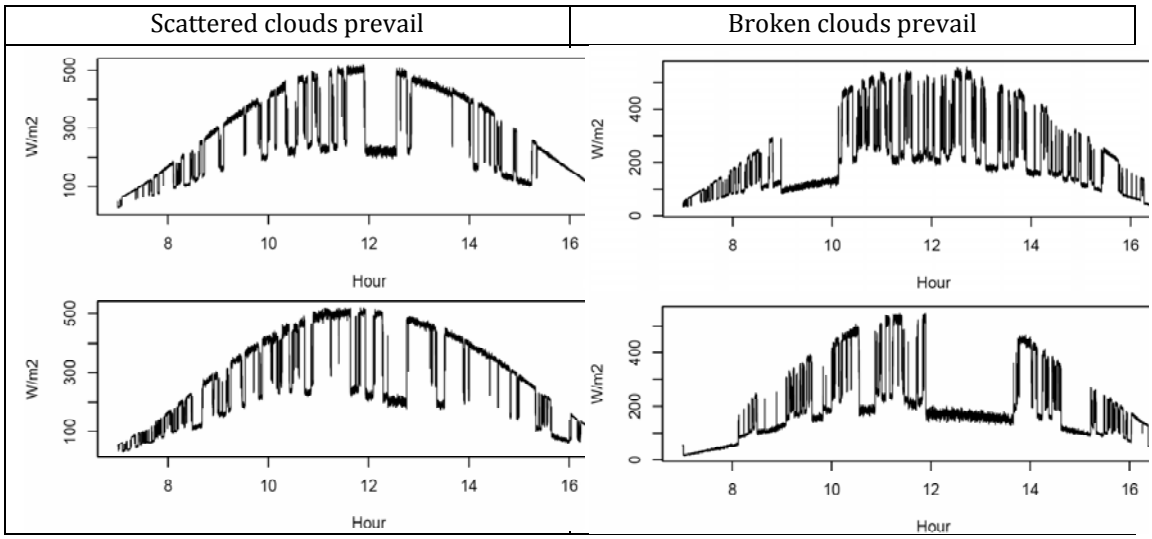

Figure 17. Mid-upper level sky condition synthetic time series.

The mixed cloud level only

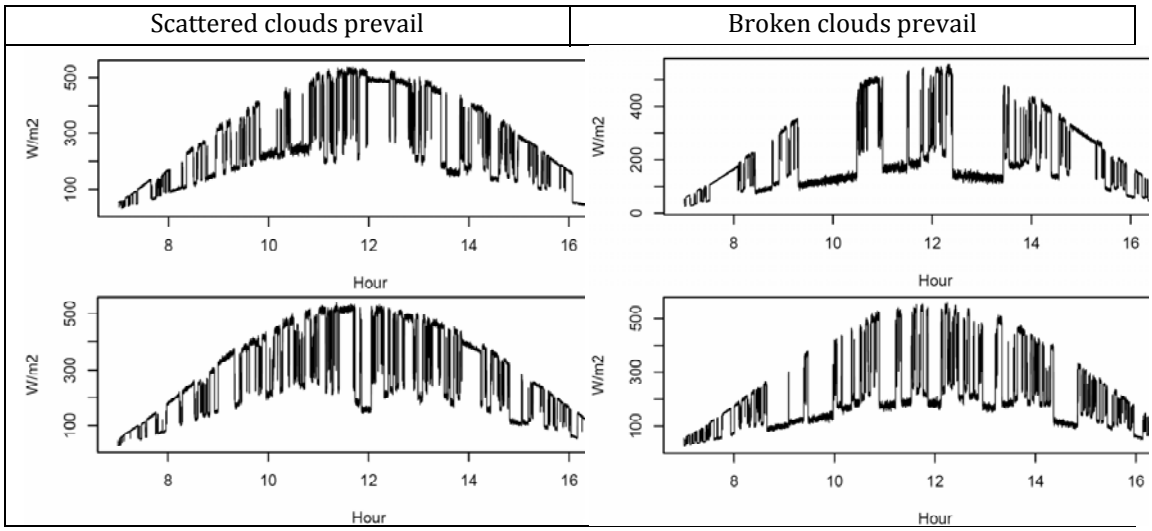

Figure 18. Mixed sky condition synthetic time series.

Growing and non-growing season analyses

The growing season is associated with the leave emergence from deciduous trees and vegetation. The start of the season is accompanied with the rapid change in the heat and moisture fluxes in mixed layer in such way that the sensible heat flux begins to fall and specific humidity and the latent heat flux increase due to vegetation evapotranspiration (Fitzjarrald et al., 2001; Freedman et al., 2001). A rapid drop in Bowen ratio with leaf emergence heralds the beginning of the growing season in the NE United States in spring followed by the growth of Bowen ratio in the fall. For Harvard Forest, the effective growing season in approximately 140th day of the year (beginning of May) and finishes in September (Sakai et al, 1997; Freedman et al, 2001; Fitzjarrald et al. 2001).

During this season the surface T and q tendencies approximately balance to maintain the relative humidity at about 50% , which maintains a nearly constant lifting condensation level height (Fitzjarrald et al., 2001). This occurs because plant evapotranspiration and more frequent occurrence of convective boundary layer cumulus clouds, which we believe serves to reduce mid-day plant water stress. So the growth season should have distinctive features with higher light and dark variability comparing to the fall-winter season and entire year.

To investigate this feature, we separated our 6-year long 1-second series on the growing season and the rest fall-winter season. As noticed above, the growing season consists of the data from May till September, and the rest is the fall-winter season. For consistency with the previous Freedman et al., 2001 work, we also made a separate look at the Pre and Post-growing season periods. In the current research the growing season is taken between 122nd and 274th day (153 days), and the rest is

non-growing season (212 days). Hence, the pre-growing season is 121 days long, and the post-growing season is 91 days long.

Scattered clouds

	All season	growing	Non growing	Pre growing	Post growing
low	21041 5035101	11327 2418759	9714 2616342	6079 1531184	3635 1085158
upper	2538 584776	1505 355210	1034 229606	711 133020	323 96586
Mix both	5 893	2 271	3 622	1 585	2 37
Mix At last one	874 212414	694 129038	180 83376	97 68132	83 15244

Broken clouds

	All season	growing	Non growing	Pre growing	Post growing
low	5782 928944	2092 347713	3691 581276	2544 365409	1148 215903
upper	3989 1090166	1451 337393	2539 752818	1645 421665	895 331189
Mix both	764 92315	471 51552	294 40808	186 19347	109 21497
Mix At least one	4683 590812	2624 326092	2059 264720	1297 160025	762 104695

Table 10. Cloud distribution among the selected seasons both by number of cases and by duration (seconds).

When scattered clouds are detected, the low-level clouds are predominant in all cases. When broken clouds are detected, the upper level clouds overtake the low-level ones, especially during the non-growing season. Due to the different lengths of the growing season (153 days) and non-growing season (212 days), the direct inter-comparison is not possible, but we still can make a direct comparison between the scattered and broken within the seasons and compare the relative occurrence of different cloud levels between the seasons.

The following diagram presents the within-the-season comparison of frequency of the cloud levels between the scattered and broken conditions:

Growing season	Non-Growing season
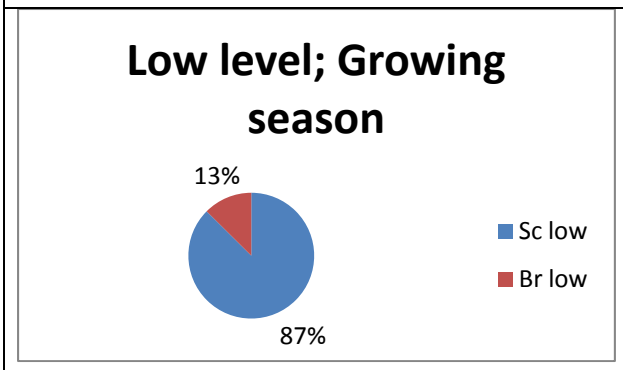	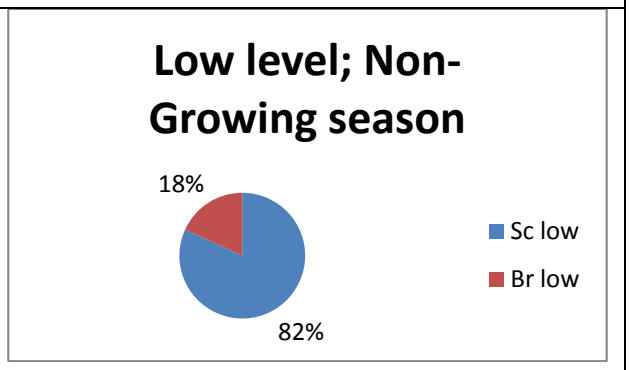
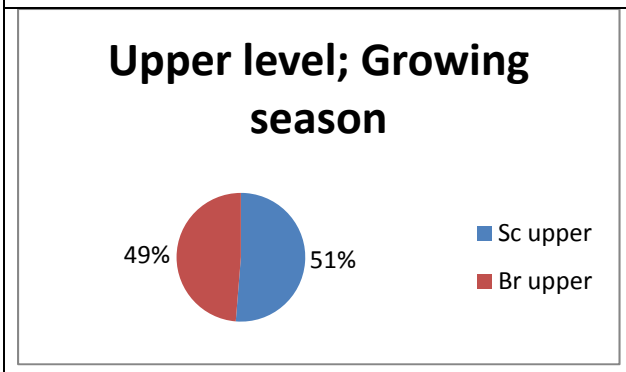	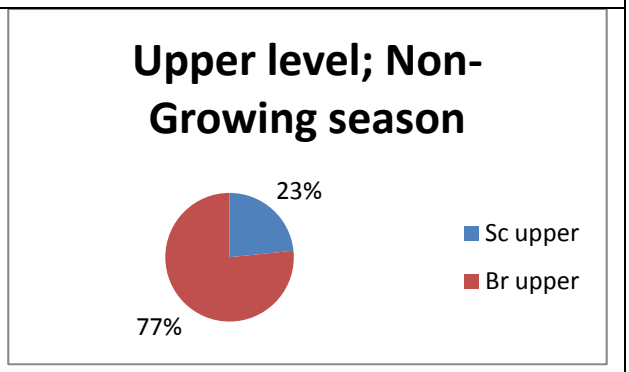
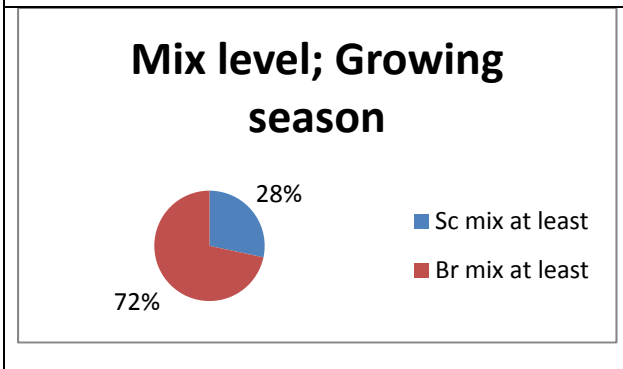	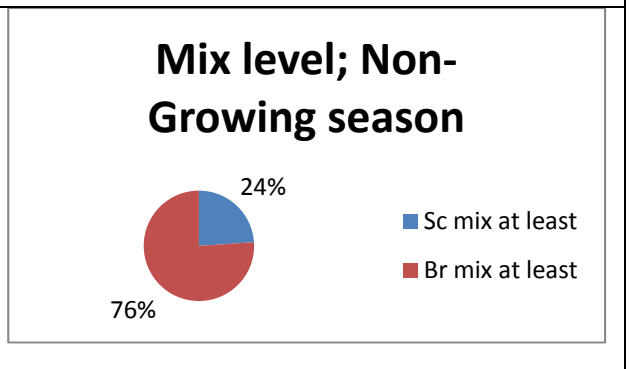

Figure 19. Seasonal pattern of the frequency of the cloud levels reported for the scattered and broken conditions.

Even though both the low-level clouds and the mixed level clouds maintain about the same proportion between scattered and broken for all seasons with a little more broken low clouds in non-growing season, upper level scattered clouds prevail during the growing season, while upper level broken clouds dominate during non-growing season.

The following cumulative diagram presents the cloud level distribution between the growing and non-growing seasons by duration:

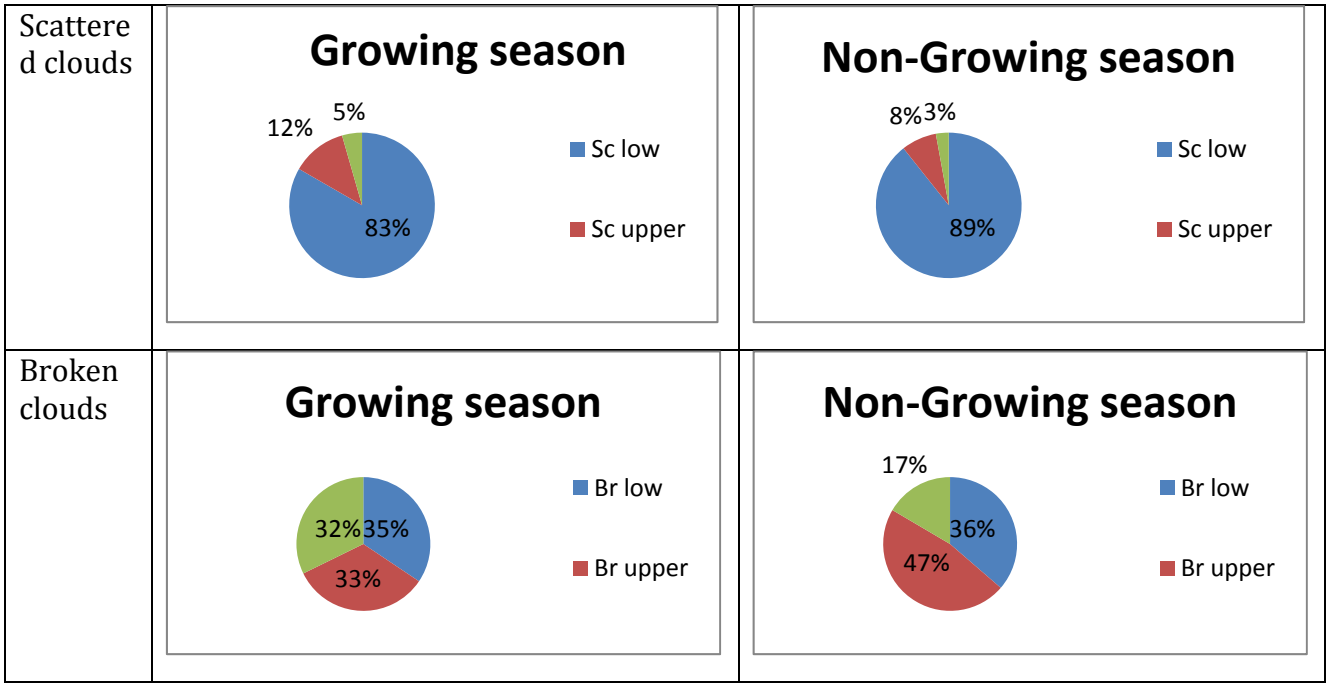

Figure 20. Cumulative diagram of the cloud level frequency distribution for growing and non-growing seasons.

Scattered cloud conditions represent by low-level clouds more than 80% of the time. The upper level clouds make about 10% of the scattered cloud conditions time, and the rest is In contrast, for *broken cloud* conditions, the presence of cloud at different levels differs between the growing and non-growing seasons. During the growing season all the cloud level and their mixing are about equally present, but during the non-growing season the upper level clouds prevails (47% of time) over the low-level clouds (36% of time), and the mix level clouds are less present.

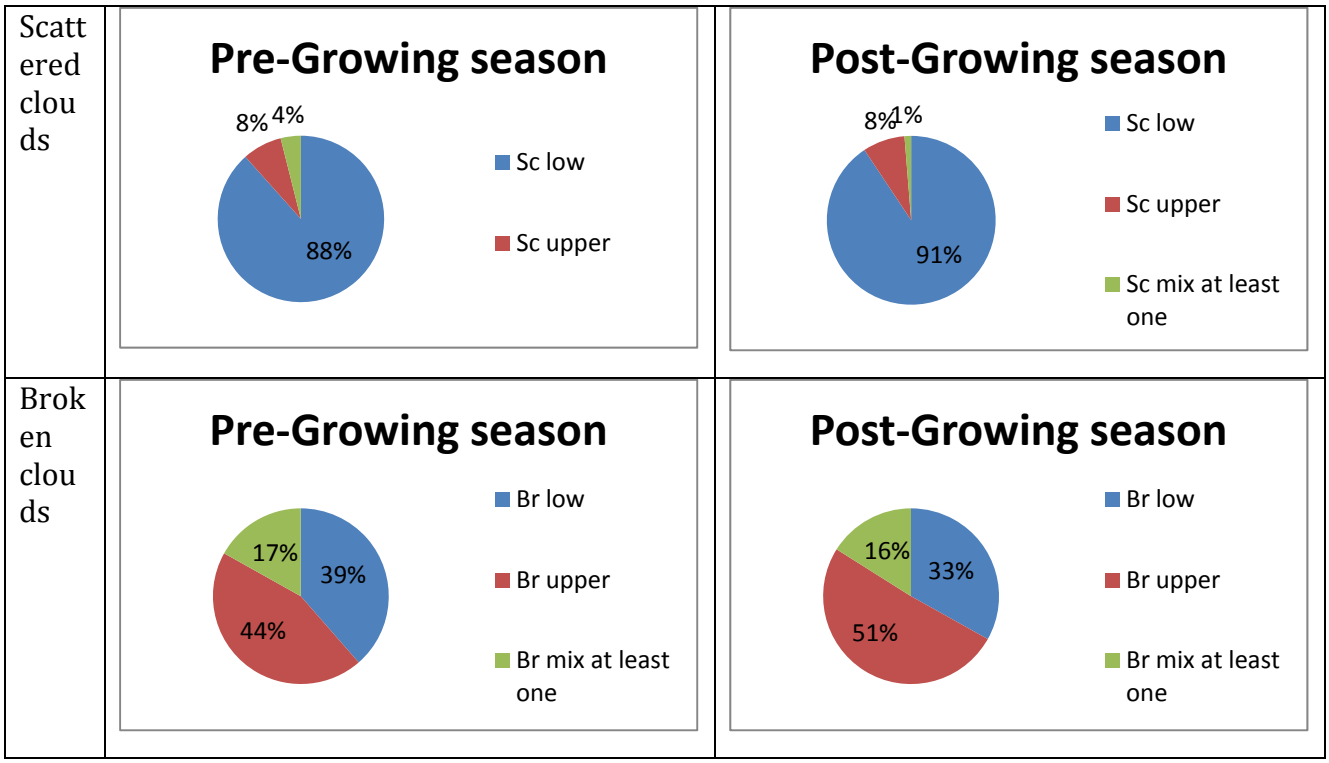

Figure 21. Cumulative diagram of the cloud level frequency distribution between the pre-growing and post-growing seasons.

The diagrams show consistent cloud level distribution between the seasons for scattered cloud conditions with predominantly low-level clouds presented. For broken cloud conditions, the upper level clouds are predominant, but the Pre-growing season has higher relative occurrence of low-level clouds than the Post-growing season, and on the contrary, the Post-growing season has higher occurrence of the upper level clouds than the Pre-growing season.

Combining the cloud occurrence on the different levels with the mean durations on the light and dark passes we found before, we can conclude that the predominant presence of low-level clouds during the scattered cloud conditions and the predominant presence of upper level broken clouds at non-growing season lead to the higher observed light variability for scattered cloud conditions at growing season than one for the broken cloud conditions at non-growing season when the cloud cover more dense and uniform.

The statistics and distributions by seasons

Following to the previous approach we present the statistics and distribution analysis by seasons.

Growing season

Low-level clouds		Mid-upper level clouds	
Scattered clouds prevail		Scattered clouds prevail	
clear	mean= 225.4502 sd= 526.9268	clear	mean= 200.2684 sd= 395.3591
cloud	mean= 105.1991 sd= 292.8009	cloud	mean= 204.7045 sd= 549.3856
Broken clouds prevail		Broken clouds prevail	
clear	mean= 100.6787 sd= 205.4549	clear	mean= 78.92504 sd= 144.6563
cloud	mean= 184.6023 sd= 473.4006	cloud	mean= 256.2927 sd= 634.7743

Table 11. Means and standard deviations for the cloud levels during the growing season.

Low-level clouds				
	Scattered clouds prevail		Broken clouds prevail	
Lognormal	clear	S= 0.06698743 P= 0	clear	S= 0.063071 P= 0.000526463
	cloud	S= 0.06412432 P= 0	cloud	S= 0.079343 P= 4.60635e-06
Weibull	clear	S= 0.01672778 P= 0.0733787	clear	S= 0.0333443 P= 0.1834406
	cloud	S= 0.0181584 P= 0.0437299	cloud	S= 0.0305637 P= 0.2667655
Mid-upper level clouds				
	Scattered clouds prevail		Broken clouds prevail	
Lognormal	clear	S= 0.092517 P= 5.40153e-06	clear	S= 0.04704517 P= 0.0906212
	cloud	S= 0.05282059 P= 0.0302742	cloud	S= 0.04720548 P= 0.0752418
Weibull	clear	S= 0.03485879 P= 0.2980189	clear	S= 0.04487425 P= 0.1105022
	cloud	S= 0.03348862 P= 0.3451332	cloud	S= 0.04364525 P= 0.1059944

Table 12. Results of Kolmogorov-Smirnov goodness of fit test on Lognormal and Weibull distributions.

Non-Growing season

Low-level clouds		Mid-upper level clouds	
Scattered clouds prevail		Scattered clouds prevail	
clear	mean= 253.9502 sd= 619.9795	clear	mean= 210.0039 sd= 557.1735

cloud	mean= 121.8572 sd= 393.0108	cloud	mean= 173.2941 sd= 472.326
Broken clouds prevail		Broken clouds prevail	
clear	mean= 80.9989 sd= 174.6784	clear	mean= 98.30105 sd= 241.824
cloud	mean= 184.8522 sd= 510.8986	cloud	mean= 262.8654 sd= 706.5661

Table 13. Means and standard deviations for the cloud levels at non-growing season.

Low-level clouds				
	Scattered clouds prevail		Broken clouds prevail	
Lognormal	clear	S= 0.0596080 P= 3.1086e-15	clear	S= 0.0533031 P= 7.8240e-05
	cloud	S= 0.0562768 P= 2.4924e-13	cloud	S= 0.0604692 P= 3.1280e-06
Weibull	clear	S= 0.018892 P= 0.05500099	clear	S= 0.02189409 P= 0.3277309
	cloud	S= 0.022526 P= 0.01370872	cloud	S= 0.0287877 P= 0.08283305
Mid-upper level clouds				
	Scattered clouds prevail		Broken clouds prevail	
Lognormal	clear	S= 0.07735439 P= 0.0041113	clear	S= 0.0553768 P= 0.00098360
	cloud	S= 0.05453729 P= 0.0890928	cloud	S= 0.0474353 P= 0.0070189
Weibull	clear	S= 0.03792537 P= 0.4249463	clear	S= 0.0293539 P= 0.2203998
	cloud	S= 0.06291591 P= 0.0247064	cloud	S= 0.0337477 P= 0.09777574

Table 14. Kolmogorov-Smirnov goodness of fit test on Lognormal and Weibull distributions.

In all the cases except for the dark passes for mid-upper level scattered clouds at non-growing season the Weibull distribution fit performs better than the Lognormal fit. So in the synthetic time series generation we'll continue using Weibull distribution as we've done it earlier.

Generating the synthetic time series

We uses the same algorithm as above to generate time series for the growing and non-growing seasons. The following Figures present the synthetic daytime series:

Growing Season

Scattered clouds prevail	Broken clouds prevail
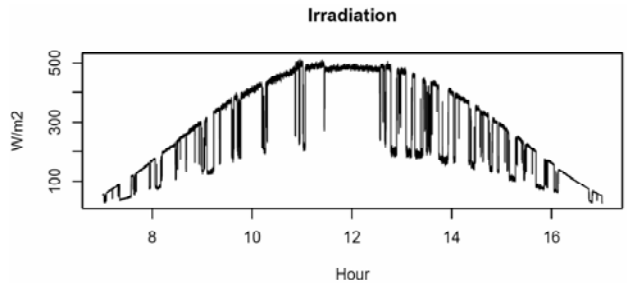	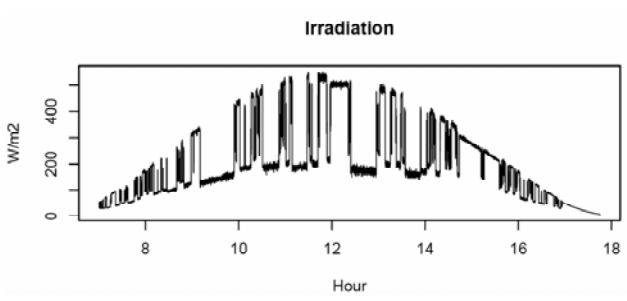

Figure 22. Synthetic times series for the growing season condition, low cloud situation.

Scattered clouds prevail	Broken clouds prevail
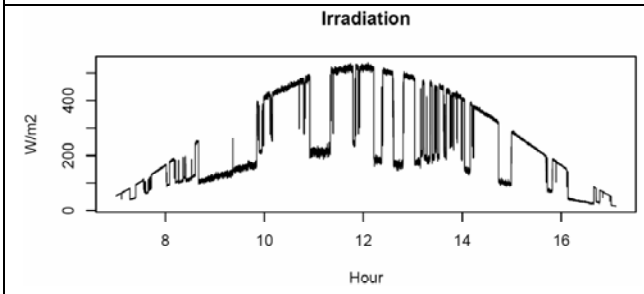	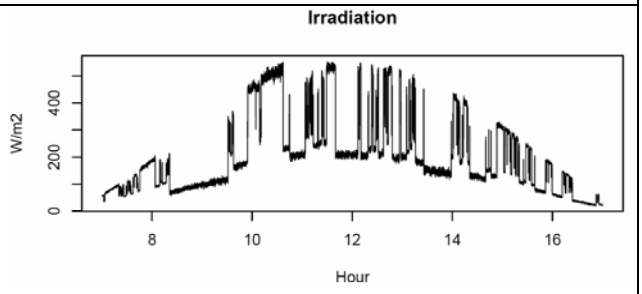

Figure 23. Synthetic times series for the growing season condition, upper cloud only situation.

Non-Growing season

Scattered clouds prevail	Broken clouds prevail
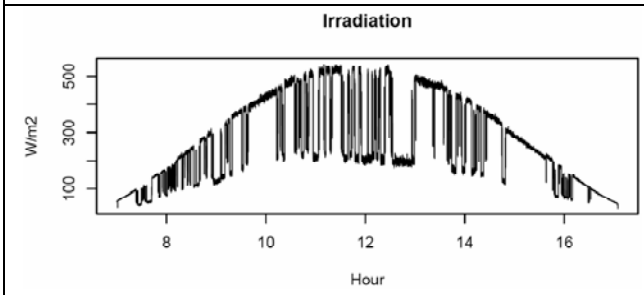	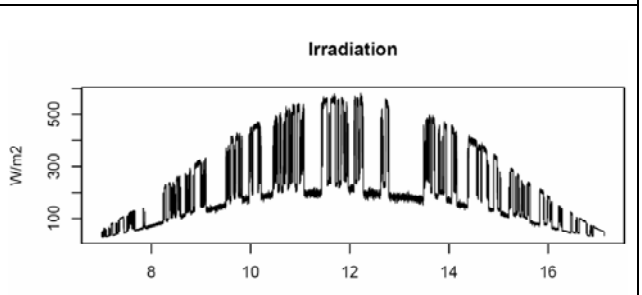

Figure 24. Synthetic times series for the non-growing season condition, low cloud only situation.

Scattered clouds prevail	Broken clouds prevail

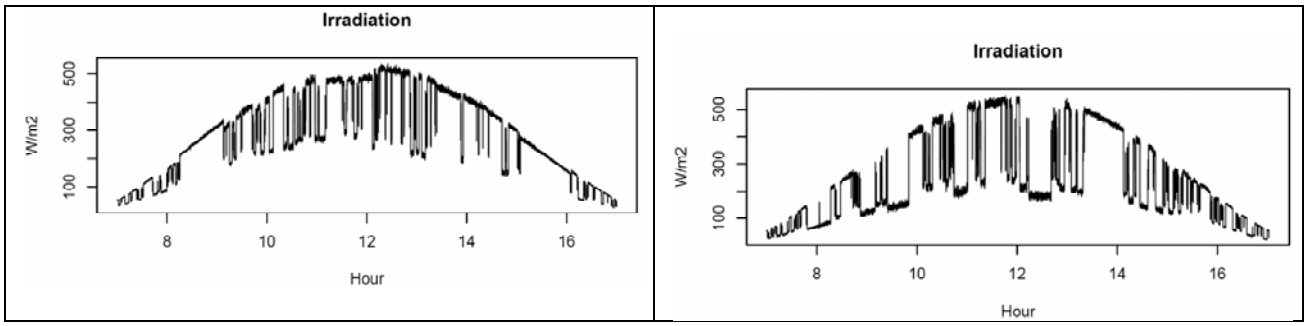

Figure 25. Synthetic times series for the non-growing season condition, upper cloud only situation.

The major drawback of this pure statistical approach of time series generation above is the rapid change of the simulated irradiances within the light or dark passes. In real conditions, there could be many different values so the variability is being held the same, but the values are distributed in more organized way so the change in irradiance occurs much slowly and at a smaller pace.

9. Conclusions

Cloud level cases studies concentrate on *scattered* and *broken* cloud conditions. In presence of the low-level clouds there is very good agreement between all-clouds cases for using the Weibull *pdf* fit to describe the distributions of light and dark periods.

In the mid-upper level cloud case, different distribution behavior is observed. The corresponding distributions are more skewed and fatter tailed, which makes them more suitable for the Lognormal *pdf* fits instead of the Weibull ones. This may occur owing to the different cloud patterns between the low-level convective clouds and the middle level frontal clouds. However, the low number of light and dark periods observed in this case doesn't fully support this conclusion.

In all cases, the scattered cloud conditions are characterized by the larger mean light pass lengths and smaller mean dark pass lengths. And for the broken cloud conditions, the mean light pass lengths are smaller than the dark ones.

10. Plans for future studies

This work helped us to understand better the light and dark distributions of light change induced by clouds in Harvard Forest. We find that the the Weibull distribution adequately describes the both light and dark interval durations.

In current research we focused on bulk sets of periods without distinguishing the periods with the similar cloud base speeds or cloud sizes. There is some ambiguity because variable winds will alter the absolute light and dark passes lengths and broad peaks in the histograms. However, these winds will have a minor of no effect on the consecutive light and dark period lengths over short intervals.

In continuing work, we will focus on the time-series and statistical relationships of light and dark and their ratios on the short scale to clear the ambiguity induced by wind change. In future work such a cloud characterization can be related to water and light use efficiency estimates for each of the three ecosystems.

The following tasks are left for future work:

1. We will use the synthetic and observed temporal forcing functions to exercise a stomatal opening/closing model following the methods of [*Ooba and Takahashi*, 2003] and [*Vico et al.*, 2011]. The ambition in this modeling exercise is to split apart the sensitivity of net carbon uptake by a forested ecosystem on cloudy days into dependence on: a) diffuse vs. direct illumination; b) reduction of heat stress owing to dark intervals during cloud passage; c) enhancement of photosynthesis during limited light intervals.

2. Installing a cloud ceilometer near the EMS tower to recover cloud base and cloud fraction. High frequency echo data will be complemented with coarser GOES satellite cloud estimates. This is to be followed by intercomparison, calibration and replacement of the radiative flux observation suite at the HF EMS tower. ***There is a pressing need to keep the EMS radiation instruments operating during the period when the new NEON tower is starting up.***

3. At the time of the *Freedman et al.* [2001] and *Fitzjarrald et al.* [2001] papers, National Weather Service Automatic Surface Observing System (ASOS) stations were still being commissioned all over the US. In future we would like to return these analyses to include the US east of the Mississippi, taking advantage of the additional decade of data from the much larger ASOS station database.

4. We will consider the correlation dimension of the varying solar radiation signal using Theiler's [1987] approach and then generate synthetic series associated with known sky types. The most promising sky types for vegetation sensitivity are likely to be the forced cumulus situations studied in [*Freedman et al.*, 2001; *Freedman and Fitzjarrald*, 2001].

5. Finally, we hope to return to our original ecological question: How does the 'cloudy day' carbon uptake depends on cloud type, cloud fraction, and season? These data will complement the ongoing subcanopy eddy CO_2, H_2O and heat flux measurements

.

11. References

Assuncão, H. F., J. F. Escobedo, A. P. Oliveira (2007): A new algorithm to estimate sky condition based on 5 minutes-averaged values of clearness index and relative optical air mass, Theor. Appl. Climatol. 90, pp. 235–248

Berg, L. K., Evgenuei I. Kassianov, Charles N. Long, and David L. Mills Jr. (2011): Surface summertime radiative forcing by sallow cumuli at the Atmospheric Radiation Measurements Southern Great Plains site, Journal of Geophysical Research 116,

Chow, C. W., B. Urquhart, M. Lave, A. Dominguez, J. Kleissl, J. Shields, and B. Washom (2011), Intra-hour forecasting with a total sky imager at the UC San Diego solar energy testbed, *Solar Energy* 85 (11), 2881-2893.

Duchon, C. E. and M. S. O'Malley (1999): Estimating Cloud Type from Pyranometer Observations, J. Appl. Meteorol. 38, 132-141

Earl J. McCartney (1976): *Optics in the Atmosphere: scattering by molecules and particles*, John Willey & Sons, New York, 408 pp.

Falconer, R. E. (1948), *A method for obtaining a continuous record of the type of clouds in the sky during the day, Final Report Project Cirrus Rep. RL 140. General Electric Research Lab., Schenectady NY*.

Falconer, R. E. (1965), A simple method for obtaining a continuous record of the presence and type of clouds in the sky during the day, *Pure and Applied Geophysics*, *60*(1), 236–244.

Fitzjarrald, D. R. and S. N. Kivalov (2012): Clouds and the temporal quality of incident light in two forested ecosystems, Terrestrial Ecosystem Science conference, April 23-24, Washington DC

David R. Fitzjarrald, Otavio C. Acevedo and Kathleen E. Moore (2001), Climate consequnces of leaf presence in the Eastern United States, Journal of Climate, 14, 598 – 614.

Freedman, J. M., and D. R. Fitzjarrald (2001), Postfrontal airmass modification, *Journal of Hydrometeorology*, *2*(4), 419–437.

Freedman, J. M., D. R. Fitzjarrald, K. E. Moore, and R. K. Sakai (2001), Boundary layer clouds and vegetation–atmosphere feedbacks, *Journal of Climate*, *14*(2), 180–197.

Lianhong Gu, Jose D. Fuentes, Michael Garstang, Julio Tota da Silva, Ryan Heitz, Jeff Sigler, Herman H. Shugart (2001): Cloud modulation of surface solar irradiance at a pasture site in southern Brazil, Agricultural and Forest Meteorology 106, pp. 117–129

Harvard Forest:
http://cdiac.esd.ornl.gov/programs/ameriflux/data_system/aaHarvard_Forest_g2.html

International Organization for Standardization, *Standard Atmosphere*, International Standard ISO2533 (1972)

Kalisch, J. and Andreas Macke (2008): Estimation of the total cloud cover with high temporal resolution and parameterization of short-term fluctuations of sea surface insolation, Meteorologische Zeitschrift, Vol. 17, # 5, pp. 603-611

Lave, Kleissl, M. J. and E. Arias-Castro (2011), High-frequency irradiance fluctuations and geographic smoothing, *Solar Energy*.

López, Raúl Erlando (1977): The Lognormal Distribution and Cumulus Cloud Populations. Mon. Wea. Rev., 105, 865–872

METAR: http://cdo.ncdc.noaa.gov/qclcd/QCLCD?prior=N

Ooba, M., and H. Takahashi (2003), Effect of asymmetric stomatal response on gas-exchange dynamics, *Ecological modelling*, *164*(1), 65–82.

Orsini, A., Claudio Tomasi, Francescopiero Calzolari, Marianna Nardino, Alessandra Cacciari, Teodoro Georgiadis (2002): Cloud cover classification through simultaneous ground-based measurements of solar and infrared radiation, Atmospheric Research 61, #4, pp. 251 – 275.

Sakai, R. K., R. Fitzjarrald and E. K. Moore (1997), Detecting leaf area and surface resistance during transition seasons, Agric. For. Meteor., 84, 273 – 284.

Segal, M. & J. Davis, (1992): The Impact of Deep Cumulus Reflection on the Ground-Level Global Irradiance. J. Appl. Meteor., 31, 217–222

Stull, R.B. (1988): *An Introduction to Boundary Layer Meteorology*, Kluwer Academic Publishers, 666 pp.

Suehrcke, H., and P. G. McCormick (1988a), The diffuse fraction of instantaneous solar radiation, *Solar Energy*, *40*(5), 423–430.

Suehrcke, H., and P. G. McCormick (1988b), The frequency distribution of instantaneous insolation values, *Solar Energy*, *40*(5), 413–422.

Theiler, J. (1987), Efficient algorithm for estimating the correlation dimension from a set of discrete points, *Physical Review A*, *36*(9), 4456.

Vico, G., S. Manzoni, S. Palmroth, and G. Katul (2011), Effects of stomatal delays on the economics of leaf gas exchange under intermittent light regimes, *New Phytologist*.

Whitehead D. and R.O. Teskey (1995): Dynamic response of stomata to changing irradiance in loblolly pine (*Pinus taeda* L.), Tree Physiology 15, pp. 245–251

Woyte, A., R. Belmans, and J. Nijs (2007), Fluctuations in instantaneous clearness index: Analysis and statistics, *Solar Energy*, *81*(2), 195–206.

Young, A. T. (1994): Air mass and refraction, Applied Optics, 33, #6, pp 1108-1110

Zillman, J. (1972): A study of some aspects of the radiation and heat budget of the Southern Hemisphere oceans. In Meteor. Stud. # 26. Bureau of Meteorology, Canberra, Australia, 526 p